A Programmable Dual-Regime Spray for Large-Scale and Custom-Designed Electronic Textiles

Taehoo Chang, Semih Akin, Min Ku Kim, Laura Murray, Bongjoong Kim, Seungse Cho, Sena Huh, Sengul Teke, Laurent Couetil,* Martin Byung-Guk Jun,* and Chi Hwan Lee*

Increasing demand for wearable healthcare synergistically advances the field of electronic textiles, or e-textiles, allowing for ambulatory monitoring of vital health signals. Despite great promise, the pragmatic deployment of e-textiles in clinical practice remains challenged due to the lack of a method in producing custom-designed e-textiles at high spatial resolution across a large area. To this end, a programmable dual-regime spray that enables the direct custom writing of functional nanoparticles into arbitrary fabrics at submillimeter resolution over meter scale is employed. The resulting e-textiles retain the intrinsic fabric properties in terms of mechanical flexibility, water-vapor permeability, and comfort against multiple uses and laundry cycles. The e-textiles tightly fit various body sizes and shapes to support the high-fidelity recording of physiological and electrophysiological signals on the skin under ambulatory conditions. Pilot field tests in a remote health-monitoring setting with a large animal, such as a horse, demonstrate the scalability and utility of the e-textiles beyond conventional devices. This approach will be suitable for the rapid prototyping of custom e-textiles tailored to meet various clinical needs.

1. Introduction

Electronic textiles, or e-textiles, are of particular interest in remote health monitoring, which enables the ambulatory monitoring of health condition or disease progression on a routine or continuous basis.[1–5] E-textiles are typically formed through the additive patterning of functional nanomaterials into fabrics in a configuration to detect physiological and electrophysiological responses on the skin.[6,7] Current approaches in producing e-textiles involve using either wet spinning, biscrolling, dip coating, screen printing, inkjet printing, dip pen nanolithography, physical vacuum depositing, or weaving to overcoat fabrics with functional nanomaterials.[8–14] In these approaches, precise control in the overcoat uniformity is a key to ensure the mechanical and electrical reliability of e-textiles during use in ambulatory health monitoring.[15,16] Despite great advances, a critical need still remains to meet the following requirements at the same time: 1) large-scale batch production through a mask-free writing of functional nanomaterials at desired shape and size; 2) seamless mechanical and electrical connection of functional nanomaterials through their deep and uniform embedment into fabrics without aggregation; 3) high spatial resolution through a fine patterning of

T. Chang, C. H. Lee
School of Materials Engineering
Purdue University
West Lafayette, IN 47907, USA
E-mail: lee2270@purdue.edu

S. Akin, B. Kim, S. Teke, M. B.-G. Jun, C. H. Lee
School of Mechanical Engineering
Purdue University
West Lafayette, IN 47907, USA
E-mail: mbgjun@purdue.edu

M. K. Kim, B. Kim, S. Cho, S. Huh, C. H. Lee
Weldon School of Biomedical Engineering
Purdue University
West Lafayette, IN 47907, USA

M. K. Kim
School of Mechanical Engineering
Hanyang University
Seoul 04763, South Korea

L. Murray, L. Couetil
Department of Veterinary Clinical Sciences
Purdue University
West Lafayette, IN 47907, USA
E-mail: couetill@purdue.edu

B. Kim
Department of Mechanical & System Design Engineering
Hongik University
Seoul 04066, South Korea

S. Teke
Secant Group LLC
Telford, PA 18969, USA

M. B.-G. Jun
Indiana Manufacturing Competitiveness Center
Purdue University
West Lafayette, IN 47907, USA

C. H. Lee
Birck Nanotechnology Center
Purdue University
West Lafayette, IN 47907, USA

**ADVANCED
SCIENCE NEWS**

www.advancedsciencenews.com

**ADVANCED
MATERIALS**

www.advmat.de

functional nanomaterials into custom sensor designs; and 4) long-term durability against multiple uses and laundry cycles. All these features are integral to the pragmatic deployment of e-textiles in clinical practice.

To this end, we introduce a unique approach that involves using a programmable dual-regime spray to produce custom-designed e-textiles at high spatial resolution (at sub-millimeter scale) across a large area (over meter scale) beyond conventional approaches. The dual-regime spray includes two separate (i.e., high- and low-speed) air flow modules on a three-axis computer numerical control (CNC) gantry.[17] This setting enables the direct custom spraying of conducting nanoparticles into arbitrary fabrics at precisely controlled mass loading and penetration depth without the need of a shadow mask or dedicated vacuum equipment that is often required in current approaches.[18,19] This setting also enables the uniform seamless coating of a waterproof elastomer over the as-sprayed conducting nanoparticles as a sealing overcoat to provide physical and chemical protection against multiple uses and laundry cycles. This study uncovered the process-structure-property relationships of various e-textiles for their implementations in a remote health monitoring setting with a large animal such as a horse.

2. Results and Discussion

2.1. Dual-Regime Spray Process

Figure 1a provides schematic illustrations of the dual-regime spray process to generate e-textiles. The corresponding photographs of this setting are shown in Figure S1, Supporting Information. The dual-regime spray process began by atomizing a 73 mm of silver nitrate ($AgNO_3$) solution in a 1:15 mixture of water and ethanol by volume into fine droplets with a pneumatic atomizer (WestMed-0210; WixOne) at a pressure of 70 kPa. The atomized droplets containing $AgNO_3$ nanoparticles were carried in a mixing chamber by a low-speed air flow (i.e., <10 m s^{-1}) to minimize cyclone effects (i.e., uniform dispersion).[17] The droplets were then passed through an internal flow-conditioning unit to sort out large droplets. At the nozzle exit, the droplets were accelerated by a high-speed (i.e., >100 m s^{-1}) central air flow to remain focused at a focal plane, thereby allowing for the narrow and deep penetration of the $AgNO_3$ nanoparticles into fabrics. Figure S2a, Supporting Information shows the cross-sectional scanning electron microscopy (SEM) and energy-dispersive X-ray spectroscopy (EDX) images of the as-sprayed $AgNO_3$ nanoparticles into a Lycra fabric to confirm their uniform seamless coating without aggregation. Figure S2b, Supporting Information shows the experimental results of multiple peeling tests using a Scotch tape (3M Inc.) to confirm the adhesion between the $AgNO_3$ nanoparticles and the fabric. No alteration in the intrinsic fabric structure was noticed during or after the dual-regime spray process. A real-time video of the dual-regime spray process is shown in Movie S1, Supporting Information.

Figure 1b shows the schematic illustrations and colored SEM images of the sprayed $AgNO_3$ nanoparticles in a Lycra fabric following subsequent overcoating of copper (Cu), Ecoflex, and gold (Au) from the left column. First, an 800 nm-thick layer of

Cu was electrolessly plated over the sprayed $AgNO_3$ nanoparticles to complete conduction paths. The electrical conductivity of the Cu overcoat increased up to 9400 S cm^{-1} after 6 h of the electroless plating, resulting in the grain size of 500 ± 37 nm on average (Figure S3, Supporting Information). For comparison, a solution of Ag nanowires (Sigma Aldrich Inc.) was also sprayed into a Lycra fabric, but at least 100 times in order to obtain a similar resistance to that of the Cu overcoat (Figure S4, Supporting Information). Thereby, the material consumption and production time in spraying the Ag nanowires were substantially higher compared to the $AgNO_3$ nanoparticles with the Cu overcoat. Next, a 60 μm-thick layer of Ecoflex was coated to seamlessly cover the conduction paths, except the areas of recording electrodes, thereby providing electrical insulation, mechanical protection, and waterproof barrier against multiple uses and laundry cycles.[20,21] Last, a 1.5 μm-thick layer of Au was electroplated over the exposed surface of the Cu overcoat (i.e., recording areas) at 5 V for a minute to promote biocompatibility and also prevent oxidation.[22,23] Figure S5, Supporting Information shows the X-ray diffraction and EDX images of the overcoat layers to confirm the uniformity. The dual regime spray process was applicable to various types of fabrics made of cotton, polyester, and Lycra without a noticeable difference in the overall coating quality (Figure S6, Supporting Information).

2.2. Optimal Operational Condition

Identifying an optimal operational condition for the dual-regime spray process is important to precisely define the line width (i.e., 0.9–10 mm), penetration depth (i.e., up to 600 μm-deep), and shape (i.e., straight or curvilinear lines) of conduction paths in fabrics. **Figure 2**a schematically illustrates the governing operational parameters of the dual-regime spray process in terms of atomization gauge pressure (P_A), nozzle transverse speed (V_N), central air velocity (V_C), and spray distance to fabrics (D_S). Figure 2b presents the effect of the governing operational parameters on spray resolution (i.e., line width) in a range of P_A = 30–150 kPa, V_N = 500–1500 mm min^{-1}, V_C = 50–120 m s^{-1}, and D_S = 2–8 mm. The spray resolution tended to increase with decreased P_A or increased V_C due to the narrow and deep interaction of the sprayed droplets with fabrics. Deep penetration throughout fabrics up to 600 μm in thickness occurred at P_A = 70 kPa and V_C = 100 m s^{-1}. The highest V_N without compromising the highest spray resolution (i.e., 0.9 mm in line width) was 1300 mm min^{-1} within a single working area (i.e., frame size of the CNC gantry) of 75 × 120 cm^2 at a time. Excessive rise in P_A or V_N beyond a threshold (i.e., >150 kPa or >1500 mm min^{-1}) resulted in disruptive or non-uniform spray patterns due to the excessively or deficiently sprayed droplets, respectively (Figure S7a, Supporting Information). The spray resolution (i.e., minimum line width) increased up to 0.9 mm with increased V_C up to 100 m s^{-1} at fixed P_A = 70 kPa and V_N = 1300 mm min^{-1} (Figure S7b, Supporting Information). Under this condition, the focal plane was formed at D_S = 2 mm. Figure 2c summarizes the experimental and computational fluid dynamics (CFD) results of the spray flow. Details of the CFD domain and local grid are shown in Figure S8a, Supporting Information. The spray flow was narrowed by the central air
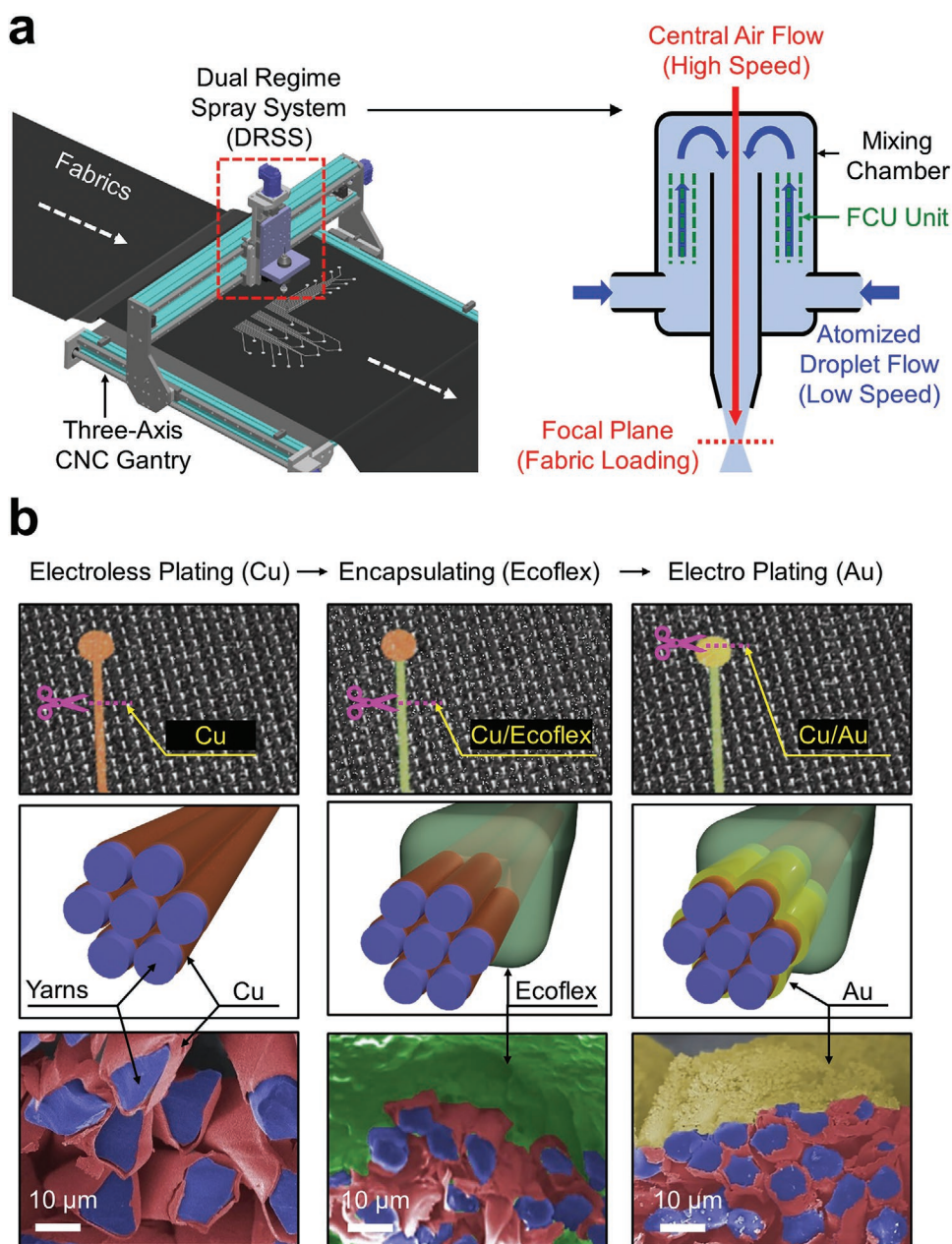
Figure 1. Dual-regime spray process. a) Schematic illustration of the dual-regime spray process using a three-axis CNC gantry. b) Schematic illustrations and colored SEM images for the subsequent overcoating of Cu, Ecoflex, and Au from the left column.

flow (i.e., $V_C = 100$ m s^{-1}) and then focused at the focal plan (i.e., $D_S = 2$ mm), which yielded the highest spray resolution at 0.9 mm. Without the central air flow (i.e., $V_C = 0$ m s^{-1}), the spray flow remained straight (Figure S8b, Supporting Information). A real-time video of the spray flow at $V_C = 0–100$ m s^{-1} is shown in Movie S2, Supporting Information. Taken together, the highest spray resolution occurred at the optimal condition of $P_A = 70$ kPa, $V_N = 1300$ mm min^{-1}, $V_C = 100$ m s^{-1}, and $D_S = 2$ mm.

Figure 2d presents the effect of P_A and D_S on mass load (left panel), penetration depth (middle panel), and electrical resistance (right panel) using test units (i.e., a conduction path in a

size of 1.3 mm × 50 mm), all of which were sprayed in a Lycra fabric. The mass load increased as P_A increased to reach the maximum (≈18 mg cm^{-2}) at $D_S = 2$ mm, which is substantially higher than those reported in previous studies.[24,25] The penetration depth also increased as P_A increased where the deep penetration (>600 μm) into fabrics occurred with $P_A \geq 70$ kPa at $D_S = 2$ mm. The high mass load and deep penetration resulted in sufficiently low electrical resistance (<2.6 Ω) at the optimal condition. The high mass load and deep penetration were mostly attributed to the kinetic energy gain of atomized droplets (i.e., ≈2.7 μm in mass median average diameter) at high atomization pressure (i.e., $P_A \geq 70$ kPa).[26] Representative

**ADVANCED
SCIENCE NEWS**

www.advancedsciencenews.com
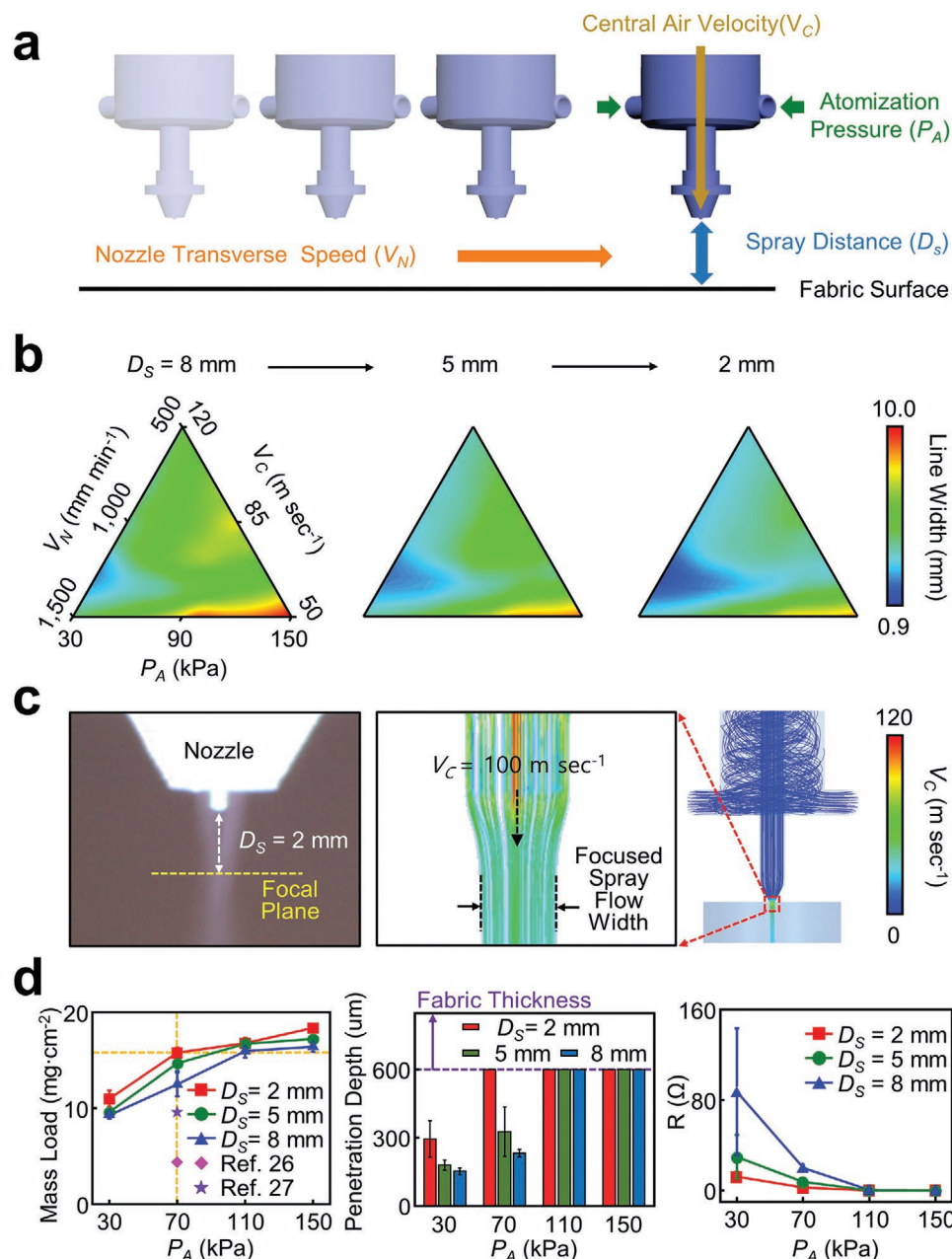
**ADVANCED
MATERIALS**

www.advmat.de

Figure 2. Optimal operational condition. a) Schematic illustration of the governing operational parameters in the dual-regime spray process. b) Effect of the governing operational parameters on spray resolution. c) Representative experimental and CFD results of the spray flow. d) Mass load, penetration depth, and electrical resistance of test units as a function of atomization pressures and spray distances.

microscopy and SEM images of the test units are shown in Figure S9, Supporting Information. Representative examples of constructing e-textiles into a resistive heater and light-emitting diodes at the optimal condition are shown in Figure S10, Supporting Information.

2.3. Benchtop Evaluations

The implementation of e-textiles in ambulatory health monitoring requires their seamless contact to the skin without delamination against periodic strain cycles (i.e., on-body movements).[27] In addition, their long-term use in clinical practice also requires a sufficient level of mechanical flexibility, water vapor permeability, and comfortability.[28–30] Commercial stretch fabrics or garments already meet all these requirements as they are breathable, durable, and intrinsically stretchable to conform to a variety of body sizes and shapes with seamless fits. Therefore, there is a particular interest in converting commercial stretch fabrics or garments into multifunctional e-textiles. To demonstrate this, the dual-regime spray process was applied to a Lycra fabric to generate test units (i.e., a conduction path
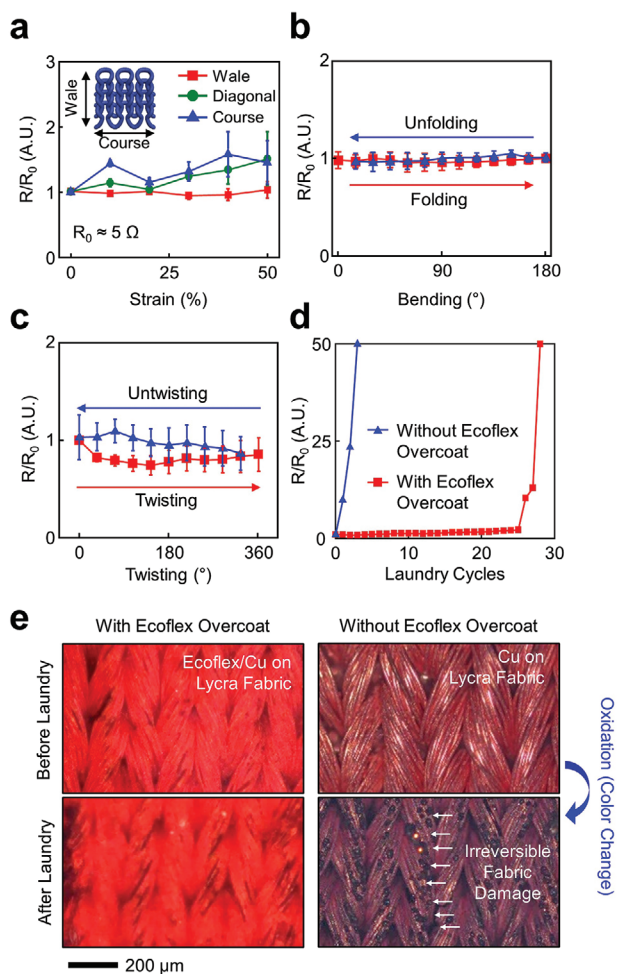
**ADVANCED
SCIENCE NEWS**

www.advancedsciencenews.com

**ADVANCED
MATERIALS**

www.advmat.de

Figure 3. Benchtop evaluations. a) R/R_0 of test units under stretching up to 50%. b) R/R_0 of test units under folding and unfolding. c) R/R_0 of test units under twisting and untwisting up to 360°. d) R/R_0 of test units under a total of multiple laundry cycles with (red line) and without (blue line) the presence of the Ecoflex overcoat. e) Microscopy images of test units before and after the laundry cycles.

in a size of 1.3 mm × 50 mm). The mechanical moduli of the test units were nearly identical as compared to the bare Lycra fabric ($E \approx 1.5$ kPa), which increased up to 6.1 kPa with the presence of the Ecoflex overcoat (Figure S11, Supporting Information). **Figure 3**a presents the relative resistance change (R/R_0) of the test units ($n = 3$ for each group) when stretched up to the intrinsic stretch limit ($\approx 50\%$) of the Lycra fabric along three different directions: 1) wale (i.e., to the lengthwise column of the meandering loops), 2) diagonal, and 3) course (i.e., to the crosswise row of the meandering loops). No substantial change in the R/R_0 appeared irrespective of the stretching direction. Irreversible fabric damages occurred when stretched beyond 50% mostly along diagonal and course directions (Figure S12a, Supporting Information), leading to an exponential increase of the R/R_0 (Figure S12b, Supporting Information). Notably, the R/R_0 barely changed when stretched even up to 150% along wale direction. This is likely attributed to the ultralow effective modulus (≈ 2.3 kPa) of the constituent "horseshoe"-like filamentary columns in the Lycra fabric that underwent large-scale,

bending-dominant deformation when stretched along wale direction.[31] Figure S13, Supporting Information shows the experimental and finite element modeling results of the single filamentary column, indicating that the maximum principal strain was 0%, 15.6%, and 38.5% at the elongation of 0%, 25%, and 50%, respectively. Consistently, the R/R_0 barely changed against folding (Figure 3b) and twisting up to 360° (Figure 3c). No noticeable differences appeared in their deformation behaviors as compared to the bare Lycra fabric (Figure S14a, Supporting Information), exhibiting a negligible or insignificant change in the R/R_0 following 1000 cycles of the deformations (Figure S14b, Supporting Information).

Figure 3d presents the impact of multiple laundry cycles on the R/R_0 with (red line) and without (blue line) the presence of the Ecoflex overcoat using a standard washing machine (Whirlpool). Each laundry cycle involved the following steps: 1) 10-min spinning in warm water at 30 °C with a fabric detergent (1 mg mL^{-1}, Jacquard Synthrapol); 2) 5-min rinsing in cold water, and 3) 2-min spin-drying at room temperature. At least 3 h sun-drying was followed for complete dry. The R/R_0 barely changed against up to 25 laundry cycles with the presence of the Ecoflex overcoat and then sharply increased with more laundry cycles due to a partial loss of the Ecoflex overcoat (Figure S15, Supporting Information). Without the presence of the Ecoflex overcoat, the R/R_0 increased immediately after each laundry cycle due to irreversible fabric damages or oxidations (i.e., color change) (Figure 3e). Importantly, the water vapor permeability of the e-textiles remained similar to that of the bare Lycra fabric when the areal fill factor of the Ecoflex overcoat remained <25% (Figure S16, Supporting Information).

2.4. Large-Scale Application in Horses

Increasing demand for remote health monitoring of farm or household animals calls for an effective wearable sensing platform to continuously collect vital health signals under ambulatory conditions.[32–34] Despite the great promise of e-textiles in this context, a rapid prototyping of custom sensor designs remains limited particularly at large scale for large animals. To address this unmet need, a pilot study was carried out using the dual-regime spray process to produce multimodal e-textiles for a large animal such as a horse. Tailored sensor designs were incorporated into commercial stretch horse blankets to support the continuous monitoring of heart activity, muscle movement, and respiration pattern in horses under ambulatory conditions. **Figure 4**a schematically depicts the envisioned concept of the remote health monitoring of horses, supported by wireless (i.e., Bluetooth) communications with a caregiver via an encrypted server. In this pilot study, standardbred female horses ($n = 2$; 11–16 years old; 417–449 kg) were included in accordance with the Purdue Institutional Animal Care and Use Committee (approved protocol number: 1111000176). The horses were considered healthy with a median body condition score of >5 out of 9 points. Prior to this study, the horses were trained to perform standardized exercises such as walking, trotting, and galloping during lunging in a round pen. The horses were housed in a stall, fed hay, and bedded on shavings.
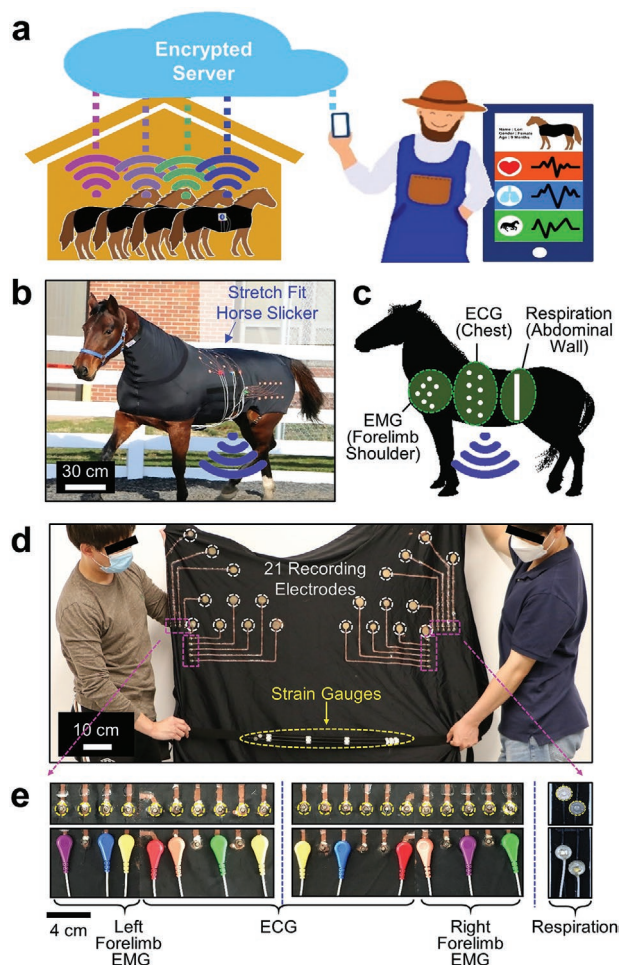
Figure 4. Large-scale application in horses. a) Schematic illustration of the envisioned concept for the ambulatory health monitoring of horses. b) Photograph of a horse in a custom e-textile. c) Measurement locations of ECG, EMG, and abdominal strain in a horse. d) Photograph of the e-textile. e) Photographs of the snap button ends in the e-textile.

Figure 4b provides a photograph of a horse in a custom e-textile built upon a commercial stretch horse blanket (Lycra fabric; Schneiders). The e-textile was configured into a tailored sensor design for the simultaneous monitoring of electrocardiogram (ECG) signals (i.e., heart activity), electromyogram (EMG) signals (i.e., muscle movement), and abdominal strains (i.e., respiration pattern) from the chest, forelimb shoulder, and abdominal wall of the horse, respectively (Figure 4c). A total of 21 recording electrodes and 2 strain gauges were rationally distributed across the entire area (100 cm × 130 cm) of the stretch horse blanket to meet specific geometric demands (Figure 4d). A total of 21 snap button ends (Florida Research Instruments) were glued using a waterproof textile adhesive (Liquid Stitch) on the peripheral edge of the stretch horse blanket in a minimally obtrusive manner (Figure 4e). The snap button ends were used for wire connections to a custom-built portable data acquisition unit (74 cm × 58 mm × 32 mm; 150 g) clipped on the stretch horse blanket. Several of the snap button ends were appropriately chosen to define desired measurement locations by considering horse-by-horse variations in body size and

shape. The portable data acquisition unit was modified from a commercial unit (BioRadio; GLNeuroTech), allowing for 1) multichannel data acquisition (up to 8 single-ended channels) at a sample rate of 250–16 000 Hz; 2) battery powering with the capacity of 420 mAh at 3.7 V; and 3) wireless (i.e., Bluetooth) data communications at 190 kbps within the maximum transmission range of 30 meters. Details of the portable data acquisition unit are shown in Figure S17, Supporting Information. Several different designs of the e-textiles were produced in various types of stretch horse blankets, including full zip blanket hood (Lycra), faceless pull-on full body blanket (Lycra), and mesh full zip blanket hood (polyester), without noticeable difference in overall quality (Figure S18, Supporting Information). For all these cases, the areal fill factor of the Ecoflex overcoat was kept at <25% in order to maintain the water vapor permeability of the e-textiles as similar as that of their bare horse blankets. As a result, no sign of discomfort was observed in the horses while freely walking, trotting, and galloping in a round pen or resting and eating in a stall (Figure S19, Supporting Information).

2.5. Pilot Field Tests in Ambulatory Health Monitoring

Figure 5a shows the representative measurement results of ECG (left panel) and EMG (right panel) signals, each of which was obtained from the upper, middle, and lower chest and the left and right forelimb shoulders of a horse under ambulatory conditions. Both the ECG and EMG signals were captured on the skin, without shaving haircoat, at a sampling rate of 1 kHz per channel with 24-bit resolution. A reference (ground) electrode was placed on tarsal bone. For the measurements, an electrolyte gel (Parker) was applied to the recording electrodes for enhanced electrical contact to the skin. The ECG signals exhibited no delay between P and QRS-waves. The recording electrodes in the e-textiles exhibited the electrical impedance of 121–442 Ω in a bandwidth of 20–500 Hz which is within a typical range of commercial recording electrodes (250–374 Ω) (Figure S20a, Supporting Information). For control measurements, commercial equine self-adhesive electrodes (H124SG; Covidien) were attached to the skin after shaving haircoat to reduce noise level (Figure S20b, Supporting Information). Notably, the e-textiles formed a seamless, tight interface with the skin under ambulatory conditions, even without the use of adhesives, thereby enabling the high-fidelity recording of ECG and EMG signals. In turn, the signal quality in terms of the amplitude, duration, and relative onset and offset times of the ECG and EMG signals was comparable between the measurements using the e-textiles and the control recording electrodes without and with shaving haircoat, respectively. Occasional motion artifacts were observed in the ECG signals during the abrupt change of body postures, which were alleviated by applying a sufficient amount (≥2 g) of the electrolyte gel.[35,36]

Figure 5b shows the representative measurement results of abdominal strains (i.e., respiration pattern) obtained using the strain gauges within the e-textiles (top panel) as compared to control measurements (bottom panel) using a conventional pneumotachograph (#4 Fleisch; EMKA Technologies). Details of the strain gauges are shown in Figure S21, Supporting Information. The gauge factor of the strain gauges was measured as
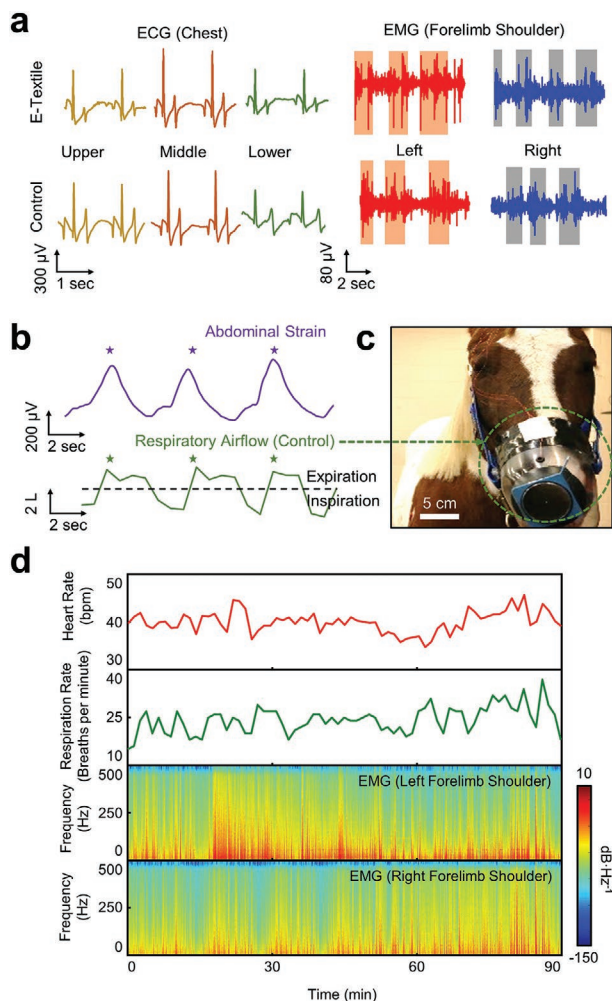
Figure 5. Pilot field tests in ambulatory health monitoring. a) Representative measurement results of ECG (left) and EMG (right) signals in a horse while walking. b) Representative measurement results of abdominal strains (top) as compared to control measurements using a conventional pneumotachograph (bottom). c) Photograph of the pneumotachograph inserted into the muzzle of a horse. d) Time-series and spectral dataset of heart rate, respiration rate, and forelimb movement in a horse while eating, wandering, and resting for 90 min. The colors indicate the amplitude spectral density.

≈5.2 at the applied strain ranging from 0% to 15%. Figure 5c shows the enlarged image of the pneumotachograph that was inserted in a facemask placed on the muzzle of the horse. The pneumotachograph was wired to an external differential pressure transducer (DP-/45-14; Validyne Engineering) while the horse was tethered still during the measurements. The tethered measurements inevitably posed discomfort and disruption in continuous recording under ambulatory conditions, as also reported in previous studies using the pneumotachograph.[37,38] Both the strain and respiratory airflow waveforms were clearly distinguishable with respect to inspiratory and expiratory abdominal movement, exhibiting the respiration rate of 12 breaths per minute under the condition. Figure 5d presents the time-series and spectral dataset of heart rate, respiration rate, and forelimb movement in the horse while resting in a stall for

90 min. The average heart rate and respiration rate were measured as 40 bpm and 24 breaths per minute, respectively. The forelimb movement was also clearly distinguishable without showing substantial motion artifacts through bandpass filtering at the cut-off frequency of 20–500 Hz.

A particular utility of the e-textiles may also exist in the routine ambulatory monitoring of cardiac and muscle activity in horse athletes to better understand exercise physiology in daily practical training.[39,40] To demonstrate this, Figure S22, Supporting Information summarizes the quantitative details of ambulatory ECG and EMG signals obtained from the chest and forelimb shoulders of a horse while trotting, walking, and resting in an arena for 15 min in a random order. The high-fidelity recording of the signals was maintained throughout the entire testing period without any sign of discomfort or skin irritation in the horse (Movie S3, Supporting Information). All the signals were simultaneously collected through multichannel data acquisitions at a sampling frequency of 1 kHz per channel from a distance via Bluetooth communications. The power consumption for the wireless monitoring was ≈50 mA with a battery life of up to 8 h on a single charge.

3. Conclusion

The results presented herein represent a unique approach in converting arbitrary fabrics into custom-designed e-textiles at high spatial resolution across a large area without significantly compromising the intrinsic fabric properties. This approach involves using a programmable dual-regime spray that enables the direct writing of custom sensor designs at substantially higher resolution (0.9 mm in line width) and conductivity (≥9400 S cm^{-1}) compared to other approaches using common sprays. The resulting e-textiles fit tightly to the body in various sizes and shapes while anchoring the recording electrodes in place under ambulatory conditions. Leveraging these features, the e-textiles provide superior measurement accuracy and fidelity in capturing physiological and electrophysiological signals over current measurement methods. Pilot field tests in a large animal, such as a horse, demonstrate the scalability and utility of the e-textiles in remote health monitoring. The established platform technology can be potentially tailored for humans in health and diseases.

4. Experimental Section

A detailed description of procedures and characterization methods is available in the Supporting Information.

Supporting Information

Supporting Information is available from the Wiley Online Library or from the author.

Acknowledgements

[1] L. Wang, X. Fu, J. He, X. Shi, T. Chen, P. Chen, B. Wang, H. Peng, *Adv. Mater.* **2020**, *32*, 1901971.

[2] J. Shi, S. Liu, L. Zhang, B. Yang, L. Shu, Y. Yang, M. Ren, Y. Wang, J. Chen, W. Chen, Y. Chai, X. Tao, *Adv. Mater.* **2020**, *32*, 1901958.

[3] W. Yan, A. Page, T. Nguyen-Dang, Y. Qu, F. Sordo, L. Wei, F. Sorin, *Adv. Mater.* **2019**, *31*, 1802348.

[4] X. Tian, P. M. Lee, Y. J. Tan, T. L. Y. Wu, H. Yao, M. Zhang, Z. Li, K. A. Ng, B. C. K. Tee, J. S. Ho, *Nat. Electron.* **2019**, *2*, 243.

[5] T.-G. La, S. Qiu, D. K. Scott, R. Bakhtiari, J. W. P. Kuziek, K. E. Mathewson, J. Rieger, H.-J. Chung, *Adv. Healthcare Mater.* **2018**, *7*, 1801033.

[6] L. Yin, K. N. Kim, J. Lv, F. Tehrani, M. Lin, Z. Lin, J.-M. Moon, J. Ma, J. Yu, S. Xu, J. Wang, *Nat. Commun.* **2021**, *12*, 1542.

[7] W. A. D. M. Jayathilaka, K. Qi, Y. Qin, A. Chinnappan, W. Serrano-García, C. Baskar, H. Wang, J. He, S. Cui, S. W. Thomas, S. Ramakrishna, *Adv. Mater.* **2019**, *31*, 1805921.

[8] K. Dong, X. Peng, Z. L. Wang, *Adv. Mater.* **2020**, *32*, 1902549.

[9] R. Cao, X. Pu, X. Du, W. Yang, J. Wang, H. Guo, S. Zhao, Z. Yuan, C. Zhang, C. Li, Z. L. Wang, *ACS Nano* **2018**, *12*, 5190.

[10] R. Guo, Y. Yu, Z. Xie, X. Liu, X. Zhou, Y. Gao, Z. Liu, F. Zhou, Y. Yang, Z. Zheng, *Adv. Mater.* **2013**, *25*, 3343.

[11] L. Hu, Y. Cui, *Energy Environ. Sci.* **2012**, *5*, 6423.

[12] S. Uzun, M. Schelling, K. Hantanasirisakul, T. S. Mathis, R. Askeland, G. Dion, Y. Gogotsi, *Small* **2021**, *17*, 2006376.

[13] Y. E. Shin, J. E. Lee, Y. Park, S. H. Hwang, H. G. Chae, H. Ko, *J. Mater. Chem. A* **2018**, *6*, 22879.

[14] T. Carey, S. Cacovich, G. Divitini, J. Ren, A. Mansouri, J. M. Kim, C. Wang, C. Ducati, R. Sordan, F. Torrisi, *Nat. Commun.* **2017**, *8*, 1202.

[15] H. Jin, N. Matsuhisa, S. Lee, M. Abbas, T. Yokota, T. Someya, *Adv. Mater.* **2017**, *29*, 1605848.

[16] N. Matsuhisa, M. Kaltenbrunner, T. Yokota, H. Jinno, K. Kuribara, T. Sekitani, T. Someya, *Nat. Commun.* **2015**, *6*, 7461.

[17] S. Akin, T. Gabor, S. Jo, H. Joe, J.-T. Tsai, Y. Park, C. H. Lee, M. S. Park, M. B.-G. Jun, *J Micro Nanomanuf* **2020**, *8*, 024511.

[18] Y. Yang, X. Wei, N. Zhang, J. Zheng, X. Chen, Q. Wen, X. Luo, C.-Y. Lee, X. Liu, X. Zhang, J. Chen, C. Tao, W. Zhang, X. Fan, *Nat. Commun.* **2021**, *12*, 1542.

[19] J. Yoon, Y. Jeong, H. Kim, S. Yoo, H. S. Jung, Y. Kim, Y. Hwang, Y. Hyun, W.-K. Hong, B. H. Lee, S.-H. Choa, H. C. Ko, *Nat. Commun.* **2016**, *7*, 11477.

[20] H. Park, J. W. Kim, S. Y. Hong, G. Lee, H. Lee, C. Song, K. Keum, Y. R. Jeong, S. W. Jin, D. S. Kim, J. S. Ha, *ACS Nano* **2019**, *13*, 10469.

[21] H. Jinno, K. Fukuda, X. Xu, S. Park, Y. Suzuki, M. Koizumi, T. Yokota, I. Osaka, K. Takimiya, T. Someya, *Nat. Energy* **2017**, *2*, 780.

[22] S. Choi, S. I. Han, D. Jung, H. J. Hwang, C. Lim, S. Bae, O. K. Park, C. M. Tschabrunn, M. Lee, S. Y. Bae, J. W. Yu, J. H. Ryu, S.-W. Lee, K. Park, P. M. Kang, W. B. Lee, R. Nezafat, T. Hyeon, D.-H. Kim, *Nat. Nanotechnol.* **2018**, *13*, 1048.

[23] E. Svanidze, T. Besara, M. Fevsi Ozaydin, C. S. Tiwary, J. K. Wang, S. Radhakrishnan, S. Mani, Y. Xin, K. Han, H. Liang, T. Siegrist, P. M. Ajayan, E. Morosan, *Sci. Adv.* **2016**, *2*, e1600319.

[24] W. Root, N. Aguiló-Aguayo, T. Pham, T. Bechtold, *Surf. Coat. Technol.* **2018**, *348*, 13.

[25] J. Landsiedel, W. Root, C. Schramm, A. Menzel, S. Witzleben, T. Bechtold, T. Pham, *Nano Res.* **2020**, *13*, 2658.

[26] J. J. Laserna, J. Moros, L. A. Álvarez-Trujillo, V. Lazic, *Appl. Opt.* **2017**, *56*, 13.

[27] H. Jin, M. O. G. Nayeem, S. Lee, N. Matsuhisa, D. Inoue, T. Yokota, D. Hashizume, T. Someya, *ACS Nano* **2019**, *13*, 7905.

[28] K.-I. Jang, S. Y. Han, S. Xu, K. E. Mathewson, Y. Zhang, J.-W. Jeong, G.-T. Kim, R. C. Webb, J. W. Lee, T. J. Dawidczyk, R. H. Kim, Y. M. Song, W.-H. Yeo, S. Kim, H. Cheng, S. Il Rhee, J. Chung, B. Kim, H. U. Chung, D. Lee, Y. Yang, M. Cho, J. G. Gaspar, R. Carbonari, M. Fabiani, G. Gratton, Y. Huang, J. A. Rogers, *Nat. Commun.* **2014**, *5*, 4779.

[29] S. Uzun, S. Seyedin, A. L. Stoltzfus, A. S. Levitt, M. Alhabeb, M. Anayee, C. J. Strobel, J. M. Razal, G. Dion, Y. Gogotsi, *Adv. Funct. Mater.* **2019**, *29*, 1905015.

[30] A. K. Yetisen, H. Qu, A. Manbachi, H. Butt, M. R. Dokmeci, J. P. Hinestroza, M. Skorobogatiy, A. Khademhosseini, S. H. Yun, *ACS Nano* **2016**, *10*, 3042.

[31] K.-I. Jang, H. U. Chung, S. Xu, C. H. Lee, H. Luan, J. Jeong, H. Cheng, G.-T. Kim, S. Y. Han, J. W. Lee, J. Kim, M. Cho, F. Miao, Y. Yang, H. N. Jung, M. Flavin, H. Liu, G. W. Kong, K. J. Yu, S. RheeII, J. Chung, B. Kim, J. W. Kwak, M. H. Yun, J. Y. Kim, Y. M. Song, U. Paik, Y. Zhang, Y. Huang, J. A. Rogers, *Nat. Commun.* **2015**, *6*, 6566.

[32] T. A. Dixon, T. C. Williams, I. S. Pretorius, *Nat. Commun.* **2021**, *12*, 388.

[33] M. Zhang, X. Wang, H. Feng, Q. Huang, X. Xiao, X. Zhang, *J. Clean. Prod.* **2021**, *312*, 127712.

[34] G. Schmidt-Traub, M. Obersteiner, A. Mosnier, *Nature* **2019**, *569*, 181.

[35] M. K. Kim, M. Kantarcigil, B. Kim, R. K. Baruah, S. Maity, Y. Park, K. Kim, S. Lee, J. B. Malandraki, S. Avlani, A. Smith, S. Sen, M. A. Alam, G. Malandraki, C. H. Lee, *Sci. Adv.* **2019**, *5*, eaay3210.

[36] Y. Khan, M. Garg, Q. Gui, M. Schadt, A. Gaikwad, D. Han, N. A. D. Yamamoto, P. Hart, R. Welte, W. Wilson, S. Czarnecki, M. Poliks, Z. Jin, K. Ghose, F. Egitto, J. Turner, A. C. Arias, *Adv. Funct. Mater.* **2016**, *26*, 8764.

[37] M. G. Arroyo, L. L. Couëtil, N. Nogradi, M. M. Kamarudin, K. M. Ivester, *J. Vet. Intern. Med.* **2016**, *30*, 1333.

[38] A. Hoffman, H. Kuehn, K. Riedelberger, R. Kupcinskas, M. B. Miskovic, *J. Appl. Physiol.* **2001**, *91*, 2767.

[39] C. C. B. M. Munsters, B. R. M. Kingma, J. van den Broek, M. M. Sloet van Oldruitenborgh-Oosterbaan, *Prev. Vet. Med.* **2020**, *179*, 105010.

[40] A. Guidi, A. Lanata, G. Valenza, E. P. Scilingo, P. Baragli, *J. Vet. Behav.* **2017**, *17*, 19.